



<b>Publication Year</b>	2018
<b>Acceptance in OA@INAF</b>	2020-09-25T12:03:09Z
<b>Title</b>	þý The Importance of the $^{13}\text{C}(\pm, n) ^{16}\text{O}$ Reaction in Asym
<b>Authors</b>	CRISTALLO, Sergio; La Cognata, M.; Massimi, C.; Best, A.; Palmerini, S.; et al.
<b>DOI</b>	10.3847/1538-4357/aac177
<b>Handle</b>	<a href="http://hdl.handle.net/20.500.12386/27485">http://hdl.handle.net/20.500.12386/27485</a>
<b>Journal</b>	THE ASTROPHYSICAL JOURNAL
<b>Number</b>	859



# The Importance of the $^{13}\text{C}(\alpha,n)^{16}\text{O}$ Reaction in Asymptotic Giant Branch Stars

S. Cristallo<sup>1,2</sup>, M. La Cognata<sup>3</sup>, C. Massimi<sup>4,5</sup>, A. Best<sup>6,7</sup>, S. Palmerini<sup>2,8</sup>, O. Straniero<sup>1,9</sup>, O. Trippella<sup>2</sup>, M. Busso<sup>2,8</sup>,  
G. F. Ciani<sup>9,10</sup>, F. Mingrone<sup>11</sup>, L. Piersanti<sup>1,2</sup>, and D. Vescovi<sup>2,10</sup>

<sup>1</sup> INAF—Osservatorio Astronomico d’Abruzzo, via M. Maggini snc, Teramo, Italy; [sergio.cristallo@inaf.it](mailto:sergio.cristallo@inaf.it)

<sup>2</sup> INFN—Sezione di Perugia, Via A. Pascoli snc, Perugia, Italy

<sup>3</sup> INFN—Laboratori Nazionali del Sud, Via S. Sofia 62, Catania, Italy

<sup>4</sup> Dipartimento di Fisica e Astronomia, Università di Bologna, Via Imerio 46, Bologna, Italy

<sup>5</sup> INFN—Sezione di Bologna, Viale Berti Pichat 6/2, Bologna, Italy

<sup>6</sup> Università degli Studi di Napoli “Federico II,” Via Cintia, Napoli, Italy

<sup>7</sup> INFN—Sezione di Napoli, Via Cintia, Napoli, Italy

<sup>8</sup> Università degli Studi di Perugia, Via A. Pascoli snc, Perugia, Italy

<sup>9</sup> INFN—Laboratori Nazionali del Gran Sasso, Via G. Acitelli 22, Assergi, Italy

<sup>10</sup> Gran Sasso Science Institute, Viale Francesco Crispi 7, L’Aquila, Italy

<sup>11</sup> CERN, Route de Meyrin 1211, Genève, France

Received 2018 March 2; revised 2018 April 27; accepted 2018 April 27; published 2018 May 30

## Abstract

Low-mass asymptotic giant branch stars are among the most important polluters of the interstellar medium. In their interiors, the main component ( $A \gtrsim 90$ ) of the slow neutron capture process (the  $s$ -process) is synthesized, the most important neutron source being the  $^{13}\text{C}(\alpha,n)^{16}\text{O}$  reaction. In this paper, we review its current experimental status, discussing possible future synergies between some experiments currently focused on the determination of its rate. Moreover, in order to determine the level of precision needed to fully characterize this reaction, we present a theoretical sensitivity study, carried out with the FUNS evolutionary stellar code and the NEWTON post-process code. We modify the rate up to a factor of 2 with respect to a reference case. We find that variations of the  $^{13}\text{C}(\alpha,n)^{16}\text{O}$  rate do not appreciably affect  $s$ -process distributions for masses above  $3 M_{\odot}$  at any metallicity. Apart from a few isotopes, in fact, the differences are always below 5%. The situation is completely different if some  $^{13}\text{C}$  burns in a convective environment: this occurs in FUNS models with  $M < 3 M_{\odot}$  at solar-like metallicities. In this case, a change of the  $^{13}\text{C}(\alpha,n)^{16}\text{O}$  reaction rate leads to nonnegligible variations of the element surface distribution (10% on average), with larger peaks for some elements (such as rubidium) and neutron-rich isotopes (such as  $^{86}\text{Kr}$  and  $^{96}\text{Zr}$ ). Larger variations are found in low-mass, low-metallicity models if protons are mixed and burned at very high temperatures. In this case, the surface abundances of the heavier elements may vary by more than a factor of 50.

*Key words:* nuclear reactions, nucleosynthesis, abundances – stars: AGB and post-AGB

## 1. Introduction

As it is widely accepted, the main and strong components of the  $s$ -process (nuclei heavier than  $A \sim 90$ ) found in the solar system material have been produced by relatively low-mass asymptotic giant branch (AGB) stars ( $1.2 < M/M_{\odot} \leq 4.0$ ), already extinct before the birth of the Sun. Their structures consist of three layers: a degenerate C-O core, a thin He-rich mantel (named He intershell), and a loose and largely convective H-rich envelope. They undergo recurrent He-shell flashes, called thermal pulses (TPs), separated by relatively long interpulse periods, during which a quiescent shell-H burning balances the energy lost by radiation from the stellar surface. In those objects, the most important neutron source is the  $^{13}\text{C}(\alpha,n)^{16}\text{O}$  reaction, which is active in the He intershell. According to the current paradigm, a  $^{13}\text{C}$  pocket forms at the beginning of each interpulse period in a small layer characterized by a variable H-abundance profile. Then, as this region contracts and warms up to  $\approx 90$ – $100$  MK,  $^{13}\text{C}$  starts capturing  $\alpha$  particles and, as a consequence, releases neutrons. A second neutron burst, more rapid than the first but only marginally contributing to the  $s$ -process nucleosynthesis, occurs during a TP, when the maximum temperature in the convective zone powered by the He flash exceeds 300 MK. In this case, neutrons are released through the  $^{22}\text{Ne}(\alpha,n)^{25}\text{Mg}$  reaction. This neutron source dominates the  $s$ -process nucleosynthesis of more massive AGB stars ( $4.0 < M/M_{\odot} < 9.0$ ).

Starting in the early 1980s, different physical processes were proposed as responsible for the synthesis of the  $^{13}\text{C}$  needed to reproduce observations. In particular, a thin transition zone containing a small amount of protons (only  $10^{-6} M_{\odot}$  of H) is needed between the He-rich mantel and the H-rich envelope at its deepest penetration during a third dredge up (TDU) episode. Then, at H reignition, a  $^{13}\text{C}$  pocket rapidly forms. Such a  $^{13}\text{C}$ , which was originally thought to be engulfed in the convective shell triggered by the following TP (see, e.g., Iben & Renzini 1983), burns in radiative conditions during the long interpulse phase (Straniero et al. 1995). As a matter of fact, the radiative  $s$ -process timescale is quite long (a few  $10^4$  yr), and low neutron densities (namely  $n_n < 10^8 \text{ cm}^{-3}$ ) are attained. Note that in spite of the low neutron density, the long timescale ensures a high enough neutron exposure to synthesize substantial  $s$ -process nuclei belonging to the main component. In the late 1990s, Gallino et al. (1998) carried out a large number of nucleosynthesis post-process calculations. However, the mass and profile of  $^{13}\text{C}$  within the pocket were treated as free parameters. In particular, the standard case, corresponding to about  $4 \times 10^{-6} M_{\odot}$  of  $^{13}\text{C}$ , provided the best reproduction of the main  $s$ -process component in the solar system. Subsequent papers confirmed the above described scheme (e.g., Goriely & Mowlavi 2000; Lugaro et al. 2003).

The question of what physical mechanism leads to the formation of the  $^{13}\text{C}$  pocket is still open. In the last 20 yr,

several hypotheses have been advanced. Herwig et al. (1997) (and also Herwig 2000) first proposed a convective overshoot operating during the TDU. Based on prescriptions derived from 2D hydrodynamical calculations of stellar convection (Freytag et al. 1996), they assumed that the convective mixing velocity decreases exponentially below the convective border. In this way, they obtained  $^{13}\text{C}$  pockets with masses of the order of  $(2-4) \times 10^{-7} M_{\odot}$  (thus, 10–20 times smaller than the standard case defined by Gallino et al. 1998). Later, Langer et al. (1999) investigated the possibility of rotational induced mixing, while Denissenkov & Tout (2003) analyzed the effect of a weak turbulence induced by gravity waves (see also Battino et al. 2016). It should be noted that all these models adopt a diffusion scheme to treat the mixing of protons into the He-rich and C-rich zone, independently on the engine of this mixing.

Straniero et al. (2006; see also Cristallo et al. 2009a) proposed a different algorithm, in which the degree of mixing scales linearly with the mixing velocity instead of quadratically as in the diffusion scheme. Then, by adopting an exponential decrease of the convective velocity, they showed that it is possible to produce  $^{13}\text{C}$  pockets larger than that obtained in previous studies and able to provide the required production of main-component *s*-process isotopes. Such a velocity profile drops as

$$v = v_{\text{CE}} \exp\left(-\frac{\Delta r}{\beta H_P}\right), \quad (1)$$

where  $\Delta r$  is the distance from the convective boundary defined by the Schwarzschild criterion,  $v_{\text{CE}}$  is the velocity at the formal convective boundary,  $H_P$  is the pressure scale height, and  $\beta$  is a free parameter (calibrated to  $\beta = 0.1$ ; see Cristallo et al. 2011). We refer to this mixing scheme as exponential velocity profile (EVEP) mixing. Later, Piersanti et al. (2013) investigated the effects induced by rotation on the evolution of the  $^{13}\text{C}$  pocket and the related *s*-process nucleosynthesis. Note that the adoption of the EVEP scheme facilitates the penetration of the convective envelope during TDU episodes. As a consequence, the model experiences TDUs when the mass of its H-exhausted core is lower (with respect to models without EVEP mixing). Then, models may become C-rich ( $\text{C}/\text{O} > 1$ ) at lower surface luminosities. Guandalini & Cristallo (2013) demonstrated that such a result well fits with the observational luminosity function of C stars.

More recently, Nucci & Busso (2014) advanced a new hypothesis about the formation of the  $^{13}\text{C}$  pocket (see also Trippella et al. 2016; Palmerini et al. 2018), suggesting that dynamo-produced buoyancy of magnetized materials could provide the necessary physical mechanisms to transport protons from the H-rich envelope into the He-C rich mantle. Magnetic instabilities also supply a sufficient transport rate capable of explaining the formation of a quite large zone with low  $^{13}\text{C}$  concentration. In this scenario, the original poloidal field of a rotating star generates a toroidal field of similar strength developing various instabilities (Parker 1960; Spruit 1999), among which is the buoyancy of magnetized structures (Schuessler 1977). The dynamics of buoyant magnetized domains is strongly dependent on the physics of the stellar environment, and it is in general very complex. However, Nucci & Busso (2014) showed that below the convective envelopes of AGB stars, special conditions are held, and the fully MHD equations can be solved exactly. Then, a simple

formula for the radial component of the buoyancy velocity can be obtained, and it describes a fast transport mechanism (see the original paper for details).

Besides the difficulties related to the adopted physical recipe, models also deal with the uncertainties related to many input quantities, among which are nuclear reaction rates. The one affecting the main neutron source, i.e.,  $^{13}\text{C}(\alpha, n)^{16}\text{O}$ , plays a relevant role. Cristallo et al. (2009a, 2011) found that in some low-mass AGB models,  $^{13}\text{C}$  may not be fully consumed during the interpulse. When this happens, the residual  $^{13}\text{C}$  is engulfed into the convective zone powered by the incoming TP and burns at a higher temperature. This additional neutron burst affects the compositions of isotopes in the neighborhood of critical branchings. Those authors showed that this process provides an excess of some radioactive nuclei, such as  $^{60}\text{Fe}$ , which has been proved to be alive in the early solar system (Mostefaoui et al. 2005; Tang & Dauphas 2012). Although such an occurrence is limited to the early TP-AGB phase of low-mass, high-metallicity models, a variation of the  $^{13}\text{C}(\alpha, n)^{16}\text{O}$  reaction rate may enhance or suppress such a process. The  $^{13}\text{C}(\alpha, n)^{16}\text{O}$  reaction may also play an important role during proton ingestion episodes (PIEs). These peculiar events, possibly occurring in the early TP-AGB phase of low-mass, low-metallicity stars, are characterized by proton engulfment in the convective shell triggered by the first fully developed TP. As a consequence of a PIE, on-flight H-burning occurs, with important consequences for the energetic stellar budget and the following (rich) *s*-process nucleosynthesis (Cristallo et al. 2009b). During this event, the energy provided by the  $^{13}\text{C}(\alpha, n)^{16}\text{O}$  reaction (plus the additional contribution from the relative neutron capture) plays a key role. Note that a similar nucleosynthesis may develop during a (very) late He-shell flash or an AGB final TP (PG 1159 spectral class or Sakurai's objects; see, e.g., Werner & Herwig 2007; Herwig et al. 2011).

In the case of radiative  $^{13}\text{C}$  burning, the Gamow peak energy of the  $^{13}\text{C}(\alpha, n)^{16}\text{O}$  reaction for the relevant AGB temperature is about 200 keV, which is well below the lower limit so far reached by direct measurements. In Section 2, we report the state of the art relative to its low-energy cross section that serves as input for a sensitivity study of the  $^{13}\text{C}(\alpha, n)^{16}\text{O}$  reaction and the related *s*-process nucleosynthesis in low-mass AGB stars. This is presented in Section 3, where two different hypotheses about the formation of the  $^{13}\text{C}$  pocket, namely the EVEP mixing and magnetic mixing, have been taken under consideration. In Section 4, we describe planned experiments that strive to improve our current knowledge. Finally, our conclusions are presented in Section 5.

## 2. State of the Art

Owing to its astrophysical importance, the  $^{13}\text{C}(\alpha, n)^{16}\text{O}$  *S*-factor<sup>12</sup> has been the subject of many studies aiming at the direct determination of its cross section or focusing on specific  $^{17}\text{O}$  states. A schematic diagram of the level scheme of  $^{17}\text{O}$  is shown in Figure 1. The  $^{13}\text{C} + \alpha$  entrance channel and the two competing exit channels  $^{16}\text{O} + n$  and  $^{17}\text{O} + \gamma$  are also represented by black arrows. The  $^{17}\text{O}$  levels near and above the  $\alpha$ -threshold of interest for AGB nucleosynthesis are marked in red.

<sup>12</sup> The astrophysical *S*-factor is defined as  $S(E) = E\sigma(E)\exp(2\pi\eta)$ , where  $\sigma(E)$  is the cross section and  $\eta$  is the Sommerfeld parameter ( $\eta = Z_1Z_2e^2/\hbar v$ ).

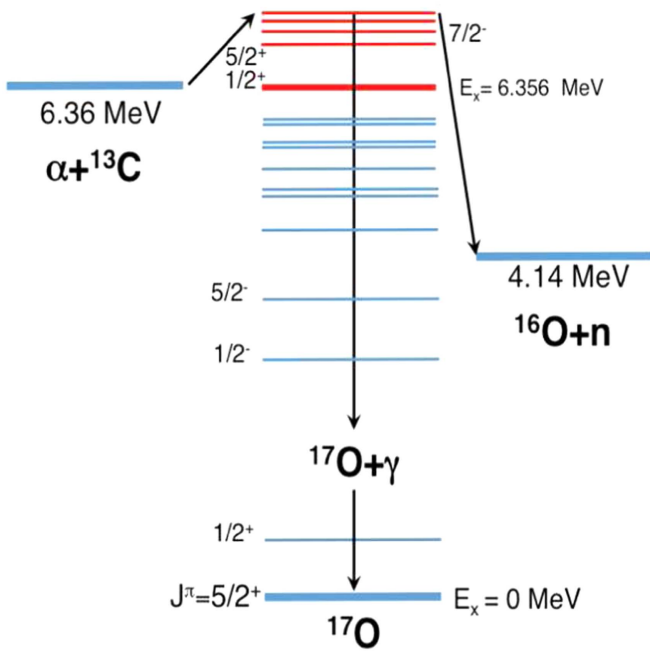


**Figure 1.** Schematic diagram of the  $^{13}\text{C}(\alpha,n)^{16}\text{O}$  nuclear reaction process, together with the competing exit channel  $^{17}\text{O}+\gamma$ . Neutrons are produced via  $\alpha$ -particle capture on  $^{13}\text{C}$  through a resonant process involving the formation of the  $^{17}\text{O}$  compound nucleus. The excited states of interest for AGB nucleosynthesis are shown in red.

Focusing on direct measurements, the most recent work by Heil et al. (2008) pointed out the substantial scatter of existing data, showing a broad (up to a factor of 2) range of absolute values for the astrophysical  $S$ -factor. On the other hand, the trend of the astrophysical  $S$ -factor as a function of energy is consistent among different data sets (Davids 1968; Bair & Haas 1973; Kellogg et al. 1989; Drotleff et al. 1993; Harissopulos et al. 2005). The lowest-energy data point sits at a center-of-mass energy of about 280 keV (Drotleff et al. 1993), slightly above the Gamow window for  $\alpha$ -induced  $^{13}\text{C}$  burning in radiative conditions. Therefore, extrapolation has proved necessary to supply a value of the reaction rate at the temperatures of astrophysical interest. The understanding of the low-energy behavior of the astrophysical  $S$ -factor is complicated by the interplay between the rise in the  $S$ -factor due to the excited state of  $^{17}\text{O}$  at  $E_x = 6.356$  MeV (ENDFS 2017) or  $E_x = 6.363$  MeV (Faestermann et al. 2015) with spin parity  $J^\pi = 1/2^+$  (see Figure 1) and the enhancement produced by the electron screening effect (Bracci et al. 1990). Moreover, such measurements are extremely challenging, since at  $\sim 300$  keV, the cross section is already as low as  $\sim 10^{-10}$  b, and the neutron detection efficiency of about 30% further reduces the signal-to-noise ratio.

Therefore, indirect measurements turned out to be very useful to constrain the  $^{17}\text{O}$  6.356 MeV level contribution. These were essentially spectroscopic measurements of the resonance energy (Faestermann et al. 2015), its squared Coulomb-modified asymptotic normalization coefficient (ANC; Johnson et al. 2006; Avila et al. 2015), and the corresponding spectroscopic factor (Keeley et al. 2003; Kubono et al. 2003; Pellegriti et al. 2008; Guo et al. 2012; Mezhevych et al. 2017), which were used to calculate the low-energy astrophysical  $S$ -factor and the  $^{13}\text{C}(\alpha,n)^{16}\text{O}$  reaction rate. Concerning these last measurements, aside from two conflicting cases (Kubono et al. 2003; Johnson et al. 2006), very different experiments and analyses supplied compatible values of

ANCs, suggesting a minor contribution of systematic errors at odds with the present status of direct measurements.

### 2.1. Exploring the Threshold Region with the Trojan Horse Method

A different approach is used by the Trojan horse method (THM; Tribble et al. 2014). Before 2015 (Faestermann et al. 2015), it was believed that the near-threshold  $1/2^+$   $^{17}\text{O}$  state was lying  $-3$  keV below the  $^{17}\text{O} \rightarrow ^{13}\text{C} + \alpha$  dissociation threshold (Tilley et al. 1993). Therefore, the THM turned out to be well suited to explore the energy interval where such resonance dominates the astrophysical  $S$ -factor (La Cognata et al. 2010). Indeed, this approach allows one to bypass several drawbacks affecting direct measurements, such as the steep drop characterizing the cross section at energies far below the Coulomb barrier and the electron screening enhancement of the astrophysical  $S$ -factor due to atomic electrons in the target (about 20% at  $\sim 300$  keV; Drotleff et al. 1993). Moreover, it offers the possibility to detect charged particles instead of neutrons (possibly leading to systematic uncertainties in the evaluation of the detection efficiency). In the THM framework, the  $^{13}\text{C}(\alpha,n)^{16}\text{O}$   $S$ -factor was deduced by investigating the  $^{13}\text{C}(\alpha,n)^{16}\text{O}$  process. Then,  $^6\text{Li}$  binding energy and  $\alpha$ - $d$  intercluster motion made it possible to reach astrophysical energies in the  $^{13}\text{C}(\alpha,n)^{16}\text{O}$  subreaction even if the THM reaction was induced at energies of many MeV per nucleon. In early THM measurements (La Cognata et al. 2012, 2013), THM data were scaled to the astrophysical  $S$ -factor recommended by Heil et al. (2008) in the  $E_{^{13}\text{C}-\alpha}$  region between  $\sim 0.6$  and 1.2 MeV. As a result, a THM  $S$ -factor in good agreement with the direct ones scaled to match the Heil et al. (2008) absolute value was attained in the 0.28–1.2 MeV energy region, and a squared Coulomb-modified ANC for the  $1/2^+$   $^{17}\text{O}$  threshold state equal to  $7.7 \pm 0.3_{\text{stat}}^{+1.6}_{-1.5\text{norm}}$  fm $^{-1}$ . This result contradicts the existing independent assessments of the ANCs, whose weighted average is  $3.9 \pm 0.5$  fm $^{-1}$  (Pellegriti et al. 2008; Guo et al. 2012; Avila et al. 2015; Mezhevych et al. 2017).

#### 2.1.1. A Concordance Scenario for the $^{13}\text{C}(\alpha,n)^{16}\text{O}$ $S$ -factor

Therefore, the pool of direct and indirect data turned out to be incoherent. Such a discrepancy could not be reconciled by taking into account the revised resonance energy, setting its center at 4.7 keV above the  $^{13}\text{C}-\alpha$  threshold (Faestermann et al. 2015). To reach a consistent  $S$ -factor, in a later THM work (Trippella & La Cognata 2017), a change of paradigm was carried out, using the existing ANC values to rescale the energy trend of the THM  $S$ -factor. Discarding the normalization in Heil et al. (2008), those authors concluded that only Bair & Haas (1973) and Drotleff et al. (1993) supplied a direct data set compatible with the THM  $S$ -factor and the ANC of the threshold level. With this new normalization, a consistent ANC of  $3.6 \pm 0.7$  fm $^{-1}$  was obtained, in turn, from the THM data. Moreover, a THM  $S$ -factor at  $E_{^{13}\text{C}-\alpha} = 140$  keV of  $1.80_{-0.17}^{+0.50} \times 10^6$  MeVb was deduced, to be compared with the astrophysical factor by Heil et al. (2008),  $S(140 \text{ keV}) = 2.2_{-0.8}^{+1.1} \times 10^6$  MeVb.

These considerations show that, at present, the main drawback of the existing data is the absolute normalization, essentially connected with neutron detection. Indirect measurements indicate that more direct data are mandatory both at low energy (below about  $\sim 0.3$  MeV, to deduce the electron

screening potential) and at higher energies (to supply a sound absolute normalization for existing direct and indirect data).

### 3. Sensitivity Study

Previous papers devoted to the analysis of the  $^{13}\text{C}(\alpha,n)^{16}\text{O}$  reaction mainly focused on the effects induced by the adoption of rates proposed by different authors. On the other hand, a sensitivity study is well suited to evaluate the expected variations on the  $s$ -process, because it allows the determination of relative distributions and, thus, the corresponding derivatives with respect to variations of the rate itself. Being the most recent direct measurement, we assume as a reference the rate proposed by Heil et al. (2008), and we vary it uniformly over the whole energy range by a factor of 1.5. In such a way, we cover most of the rates presented in the literature so far. The two most extreme cases, i.e., those proposed by Kubono et al. (2003) and Caughlan & Fowler (1988), are taken into account by varying the reference rate by a factor of 2.

As already highlighted in Section 1, the identification of the physical mechanism leading to the formation of the main  $^{13}\text{C}$  reservoir in AGB stars (the so-called  $^{13}\text{C}$  pocket) is a scientific issue debated since the end of the 1980s. No consensus has been reached on this topic to date, with different processes proposed so far: opacity EVEC mixing (Straniero et al. 2006; Cristallo et al. 2009a), magnetic buoyancy (Nucci & Busso 2014; Trippella et al. 2016; Palmerini et al. 2018), and Kelvin–Helmholtz instability coupled to gravity waves (Battino et al. 2016). These approaches lead to similar (at first glance)  $s$ -process distributions; however, their comparison is not the main goal of this paper.

Hereafter, we concentrate on  $s$ -process nucleosynthesis variations induced by the adoption of a modified  $^{13}\text{C}(\alpha,n)^{16}\text{O}$  rate in models with various masses and metallicities, computed with different codes. We analyze two sets of AGB models.

1. FUNS<sup>13</sup> evolutionary models: 1.5 and 3.0  $M_{\odot}$  with  $[\text{Fe}/\text{H}] = -0.15$  (corresponding to  $Z = 10^{-2}$ , slightly lower than the initial solar metallicity  $Z_{\odot} = 1.38 \times 10^{-2}$ ), 4.0  $M_{\odot}$  with  $[\text{Fe}/\text{H}] = -2.15$  ( $Z = 2.45 \times 10^{-4}$ , considering an initial enrichment of  $\alpha$ -elements  $[\alpha/\text{Fe}] = 0.5$ ), and 1.3  $M_{\odot}$  with  $[\text{Fe}/\text{H}] = -2.85$  ( $Z = 4.9 \times 10^{-5}$ , considering an initial enrichment of  $\alpha$ -elements  $[\alpha/\text{Fe}] = 0.5$ ).
2. NEWTON post-process calculations on a 2.0  $M_{\odot}$  with  $[\text{Fe}/\text{H}] = -0.15$  using AGB stellar structures computed with the FRANEC<sup>14</sup> code (i.e., adopting a pure Schwarzschild criterion for the identification of convective borders). Models of this kind were illustrated by, e.g., Straniero et al. (2003).

#### 3.1. FUNS Models

A detailed description of FUNS models can be found in Cristallo et al. (2016) and references therein. FUNS is derived from the FRANEC code (Chieffi & Straniero 1989). Major improvements with respect to previous versions of the code are the mass-loss law, the use of a full nuclear network (from hydrogen to bismuth) directly coupled to the physical evolution of the model, and the use of an exponentially decaying profile

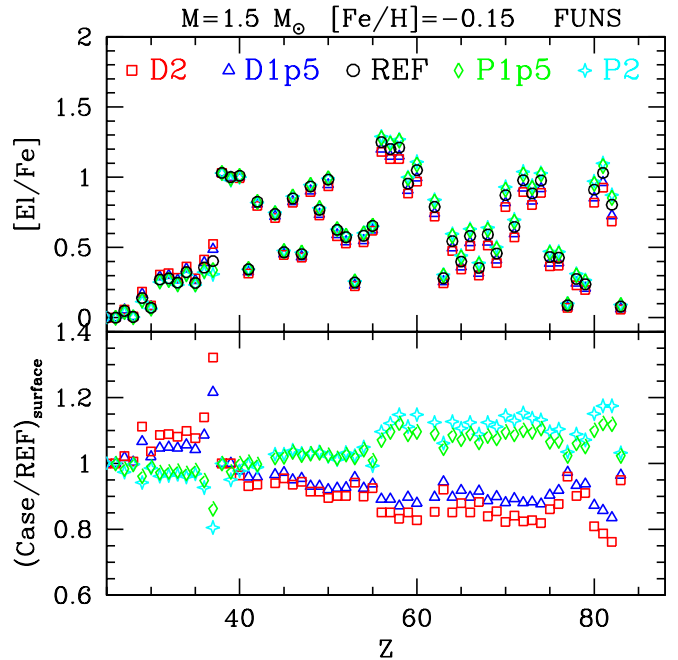


**Figure 2.** FUNS heavy-element surface distribution for an AGB star with initial mass  $M = 1.5 M_{\odot}$  and  $[\text{Fe}/\text{H}] = -0.15$ . Various symbols relate to different choices for the  $^{13}\text{C}(\alpha,n)^{16}\text{O}$  rate (see text for details).

of convective velocities at the inner border of the envelope (see Straniero et al. 2006 for details). As already reported in Section 1, the introduction of such an algorithm has deep consequences for the physical and chemical evolution of the model: it makes the border stable against perturbations, increases the efficiency of TDU episodes, and allows the formation of a tiny  $^{13}\text{C}$ -rich region (the  $^{13}\text{C}$  pocket) at the base of the envelope after each TDU. Note that the external region of the  $^{13}\text{C}$  pocket is  $^{14}\text{N}$ -rich, due to the larger number of available protons at the H-shell reignition. Such an isotope acts as a major neutron poison via the  $^{14}\text{N}(n,p)^{14}\text{C}$  reaction, thus reducing the number of neutrons available for the synthesis of heavy elements.

##### 3.1.1. Solar-like Metallicity

In this section, we discuss the effects induced by a change of the  $^{13}\text{C}(\alpha,n)^{16}\text{O}$  reaction rate in models of low mass (1.5 and 3.0  $M_{\odot}$ ) and  $[\text{Fe}/\text{H}] = -0.15$ . This metallicity is representative of the environment where pre-solar SiC grains formed. Those  $\mu\text{m}$ -sized particles are relics of the nucleosynthesis in the interiors of already extinct AGB stars, whose material polluted the solar system before its formation (see, e.g., Busso et al. 1999). The isotopic anomalies detected in those grains are, in fact, clearly connected to physical conditions not available in the solar system at the epoch of its formation. In the upper panel of Figure 2, we report the heavy-element ( $Z > 25$ ) surface composition of a star with  $M = 1.5 M_{\odot}$  and  $[\text{Fe}/\text{H}] = -0.15$ .<sup>15</sup> Symbols refer to the different adopted rates for the  $^{13}\text{C}(\alpha,n)^{16}\text{O}$  reaction: reference case (REF; Heil et al. 2008; black circles), reference case divided by a factor of 2 (D2; red squares), reference case divided by a factor of 1.5 (D1p5; blue triangles), reference case multiplied by a factor of 1.5 (P1p5; green diamonds), and reference case multiplied by a

<sup>13</sup> Software: Full Network Stellar (Straniero et al. 2006).

<sup>14</sup> Software: Frascati RApson-Newton Evolutionary Code (Chieffi & Straniero 1989).

<sup>15</sup> The spectroscopic notation is adopted:  $[\text{El}/\text{Fe}] = \log(N(\text{El})/N(\text{Fe}))_{\text{star}} - \log(N(\text{El})/N(\text{Fe}))_{\odot}$ .

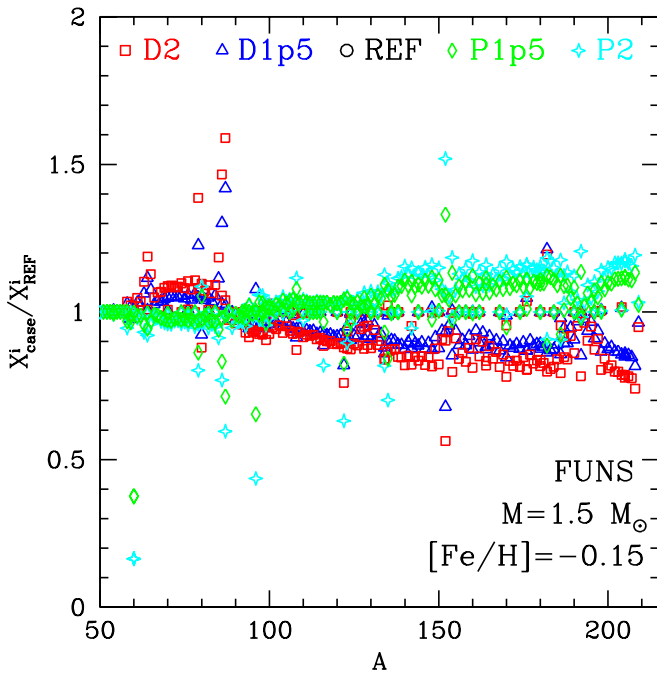


Figure 3. Same as Figure 2, but for the isotopic composition.

factor of 2 (P2; cyan stars). The corresponding isotopic surface distributions are plotted in Figure 3. An inspection of the surface elemental composition of the REF model reveals an almost flat overproduction of the three  $s$ -process peaks (upper panel of Figure 2), namely the  $ls$  component (Sr–Y–Zr), the  $hs$  component (Ba–La–Ce–Pr–Nd), and lead. An increase of the  $^{13}\text{C}(\alpha, n)^{16}\text{O}$  reaction leads to a larger production of  $hs$  elements ( $\sim 15\%$ ) and an even slightly higher synthesis of lead ( $\sim 20\%$ ).<sup>16</sup> On the contrary, elements lighter than strontium are slightly underproduced. At first glance, this result could appear in contrast to the fact that the  $^{13}\text{C}$  in the pocket fully burns in radiative conditions between two TPs (Straniero et al. 1995). Actually, this is true for most of the AGB models, but it does not hold for low-mass stars ( $M < 3.0 M_{\odot}$ ) at solar-like metallicities ( $[\text{Fe}/\text{H}] \geq -0.15$ ). In fact, Cristallo et al. (2009a) demonstrated that, for those models, part of the  $^{13}\text{C}$  in the first pockets is engulfed in the convective shell generated by the following TP (see also Karakas et al. 2010). This derives from the fact that the  $^{13}\text{C}$  in the pocket does not have enough time to fully burn in a radiative environment. Instead, AGB models with larger initial masses have high enough internal temperatures to guarantee a complete radiative  $^{13}\text{C}$  burning before the onset of the following TP. Such a behavior is easily understood by inspecting the masses of the H-exhausted cores ( $M_{\text{H}}$ ) at the beginning of the TP-AGB phase. At solar-like metallicities, stars with  $M < 3 M_{\odot}$  have almost the same  $M_{\text{H}}$ , while in more massive stars,  $M_{\text{H}}$  linearly grows with the stellar mass (see, e.g., Figure 2 of Cristallo et al. 2015). The larger the  $M_{\text{H}}$ , the larger the temperature in the He-intershell region. In addition, the lower the metallicity, the larger the  $M_{\text{H}}$ . Therefore, the convective  $^{13}\text{C}$  burning disappears with increasing the stellar mass and/or decreasing the initial metal content. When some  $^{13}\text{C}$  is ingested in the TP, it burns at a definitely

<sup>16</sup> Bismuth does not show a comparable increase due to the very low neutron capture cross section of  $^{208}\text{Pb}$ , which strongly limits  $^{209}\text{Bi}$  production at solar-like metallicities.

higher temperature, producing rather large neutron densities ( $\sim 10^{11} \text{ cm}^{-3}$ ). During that episode, the production of heavier elements is disfavored by convection, which does not allow isotopes to locally pile up. Moreover, the abundant  $^{14}\text{N}$  in the upper region of the  $^{13}\text{C}$  pocket acts as a neutron poison (via the  $^{14}\text{N}(n, p)^{14}\text{C}$  reaction), thus further decreasing the number of neutrons available for the nucleosynthesis of elements heavier than iron. Another interesting feature of convective  $^{13}\text{C}$  burning is that the production of neutron-rich isotopes close to  $s$ -process branchings largely increases with respect to standard radiative  $^{13}\text{C}$  burning. This is the case, for instance, for  $^{60}\text{Fe}$  (the largest variation, almost a factor 20, is found for this isotope),  $^{86}\text{Kr}$ ,  $^{87}\text{Rb}$ , and  $^{96}\text{Zr}$  (see Figure 3). On the contrary, other isotopes are overproduced with a large  $^{13}\text{C}(\alpha, n)^{16}\text{O}$  rate. For example, the production of  $^{152}\text{Gd}$  increases by more than 50% when the rate is multiplied by a factor of 2. This is due to the fact that the nucleosynthesis of such an isotope strongly depends on the  $^{151}\text{Sm}$  branching, which is open during standard radiative  $^{13}\text{C}$  burning (thus,  $^{152}\text{Gd}$  is partly fed by the main  $s$ -process flow). On the contrary, this branching is closed at high temperatures, as it occurs during convective  $^{13}\text{C}$  burning.<sup>17</sup> The increased production of  $^{87}\text{Rb}$  characterizing the D1p5 and D2 cases leads to the largest element surface variation, which is found for rubidium (+30%). In principle, the observed Rb/Sr ratio in C-rich stars belonging to the Galactic disk could be used to constrain the efficiency of the  $^{13}\text{C}(\alpha, n)^{16}\text{O}$  reaction. Unfortunately, the mass of those stars is poorly determined; moreover, current observational uncertainties are of the same order of magnitude of the theoretical differences just described. Thus, from this analysis, only extremely low values for the  $^{13}\text{C}(\alpha, n)^{16}\text{O}$  reaction can be safely discarded. More precise hints on the efficiency of the  $^{13}\text{C}(\alpha, n)^{16}\text{O}$  reaction can be derived from the analysis of isotopic ratios in pre-solar SiC grains. In Figure 4, we compare FRUITY models with available laboratory measurements of selected key elements<sup>18</sup> (Liu et al. 2014a, 2014b, 2015; Trappitsch et al. 2018). Note that we are evaluating the effects induced by a change of the  $^{13}\text{C}(\alpha, n)^{16}\text{O}$  rate and not the capability of the model to reproduce SiC data. The largest variations are found for  $^{64}\text{Ni}$  and  $^{96}\text{Zr}$ . This is somewhat expected, as both are neutron-rich isotopes whose production depends on an  $s$ -process branching (at  $^{63}\text{Ni}$  and  $^{95}\text{Zr}$ , respectively).

Finally, we highlight that the D2 and D1p5 models show particularly large  $^{86}\text{Kr}/^{82}\text{Kr}$  ratios ( $\sim 1$ ) with respect to the REF case (0.8), possibly giving hints on the implantation energy of the  $^{86}\text{Kr}$ -rich component (see Raut et al. 2013). In Table 1, we report the  $^{86}\text{Kr}/^{82}\text{Kr}$  and  $^{96}\text{Zr}/^{94}\text{Zr}$  number ratios of the computed models, together with their percentage variations with respect to the reference case.

In Figures 5–7, we performed the same analysis already described but for a star with initial mass  $M = 3 M_{\odot}$  and the same metallicity ( $[\text{Fe}/\text{H}] = -0.15$ ). The heavy-element distributions are almost indistinguishable, apart from the D2 case, which is characterized by a small (5%) underproduction of the heaviest elements ( $Z > 50$ ). The same holds for the isotopic composition, where the only noticeable differences are found for  $^{60}\text{Fe}$  and  $^{152}\text{Gd}$  (in any case below 10%). The theoretical

<sup>17</sup> For the interested reader, we refer to Bisterzo et al. (2015), where all branchings of the  $s$ -process are described in detail.

<sup>18</sup> The usual meteoritic notation is used:  $\delta(^nX_Z) = ((^nX_Z/{}^mX_Z)_{\text{grain}} / (^nX_Z/{}^mX_Z)_{\text{Sun}} - 1) * 1000\%$ .

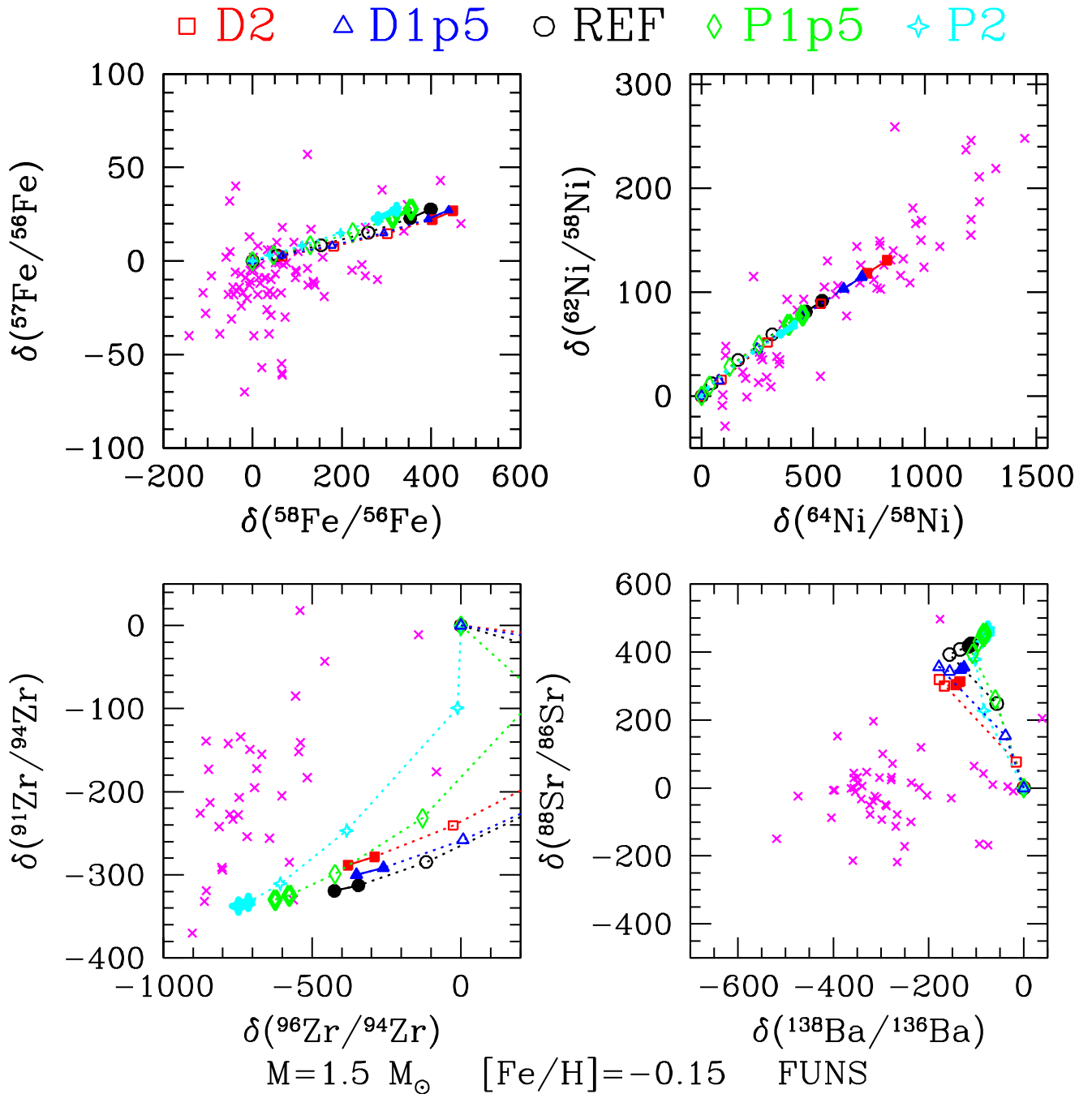


**Figure 4.** Comparison between measured isotopic anomalies for various elements compared to a model with  $M = 1.5 M_{\odot}$ ,  $[Fe/H] = -0.15$ , and different choices for the  $^{13}\text{C}(\alpha, n)^{16}\text{O}$  rate (see the text for details).

**Table 1**  
 $^{86}\text{Kr}/^{82}\text{Kr}$  and  $^{96}\text{Zr}/^{94}\text{Zr}$  Number Ratios of the  $1.5 M_{\odot}$  Model with  $[Fe/H] = -0.15$  for Different  $^{13}\text{C}(\alpha, n)^{16}\text{O}$  Rates, Together with Their Percentage Variations with Respect to the Reference Case

Case	$^{86}\text{Kr}/^{82}\text{Kr}$	$^{96}\text{Zr}/^{94}\text{Zr}$
D2	1.046 (+34%)	0.999 (+8%)
D1p5	0.966 (+24%)	0.107 (+13%)
REF	0.777	0.093
P1p5	0.669 (-14%)	0.061 (-35%)
P2	0.633 (-19%)	0.041 (-56%)

isotopic  $\delta$  curves do not evidence any appreciable deviation from the reference case. This behavior confirms that, in more massive AGBs, the temperature of the He-intershell region is always large enough to allow a complete  $^{13}\text{C}$  burning during the radiative interpulse phase. As highlighted before, this is a consequence of the larger core mass of the  $3.0 M_{\odot}$  model at the first TP followed by TDU ( $M_{\text{H}} \sim 0.59 M_{\odot}$ ), with respect to the  $1.5 M_{\odot}$  model ( $M_{\text{H}} \sim 0.56 M_{\odot}$ ).

Straniero et al. (2014) first demonstrated that the  $s$ -process-enriched ejecta of an early generation of massive AGBs may be responsible for the  $s$ -rich distributions observed in samples of

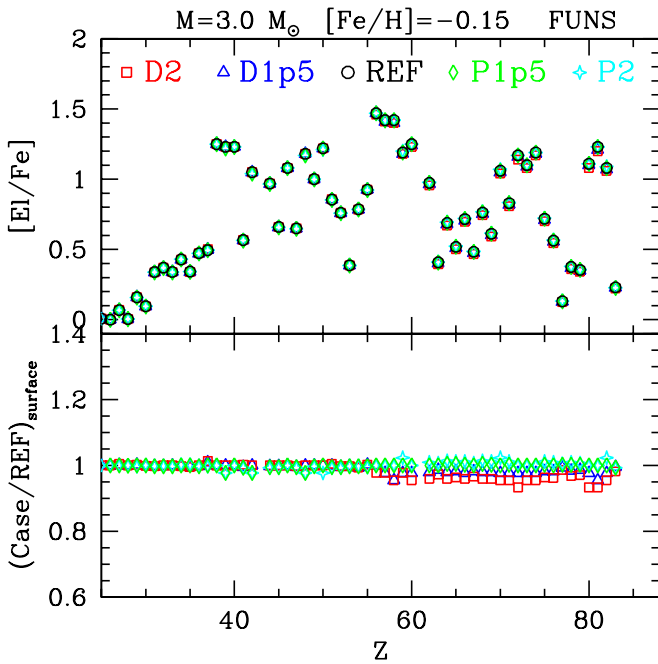


Figure 5. Same as Figure 2, but for a star with initial mass  $M = 3 M_{\odot}$ .

red giant stars belonging to the globular clusters M4 and M22 (see also Shingles et al. 2014). Those authors found that a satisfactory match to observations can be obtained, with some noticeable exceptions. In particular, theoretical models produce too much lead with respect to observations. Massimi et al. (2017) highlighted that a variation of the  $^{22}\text{Ne}(\alpha,n)^{25}\text{Mg}$  rate may soften the current disagreement between theory and observations. Here we check if the variation of the  $^{13}\text{C}(\alpha,n)^{16}\text{O}$  rate may have some effects on lead (mainly  $^{208}\text{Pb}$ ) production. To that purpose, we calculate an AGB model with initial mass  $M = 4 M_{\odot}$  and  $[\text{Fe}/\text{H}] = -2.15$ . Objects like this are thought to be the typical polluters for those stellar systems. We find that the model is not sensitive to any variation of the rate (see Figure 8). This result confirms the trend already highlighted for the  $M = 3 M_{\odot}$  model at higher metallicity (note that for this model,  $M_{\text{H}} \sim 0.86 M_{\odot}$ ).

The situation is definitely different if protons are mixed within the convective shell generated by a TP. Those types of events may occur at the first fully developed TP of low-mass, low-metallicity stars or during a very late TP near the tip of the AGB (Sakurai’s objects). As representative of this class of events, we analyze a low-mass ( $M = 1.3 M_{\odot}$ ) model at very low metallicity (e.g.,  $[\text{Fe}/\text{H}] = -2.85$ ). At this  $Z$ , the H-shell entropy barrier is weaker and, as a consequence, some hydrogen may be engulfed in the growing convective shell triggered by a TP. Due to the large temperatures, protons are captured by the abundant  $^{12}\text{C}$  while they are mixed. On the contrary, the corresponding products ( $^{13}\text{C}$  and, eventually,  $^{14}\text{N}$ ), reach the base of the convective shell, where  $T \sim 230$  MK. Thus,  $^{13}\text{C}$  is exposed to a temperature well beyond the threshold activation for the  $^{13}\text{C}(\alpha,n)^{16}\text{O}$  reaction ( $\sim 100$  MK). As a consequence, an efficient  $s$ -process takes place. After some months, the energy deposited by the on-flight burning of protons leads to the splitting of the convective shell. From that moment on, the upper shell is triggered by incomplete CNO burning, while the lower shell is sustained by the  $3\alpha$  and  $^{13}\text{C}(\alpha,n)^{16}\text{O}$  reactions. Cristallo et al. (2009b) demonstrated that, in order to properly model such a PIE, the

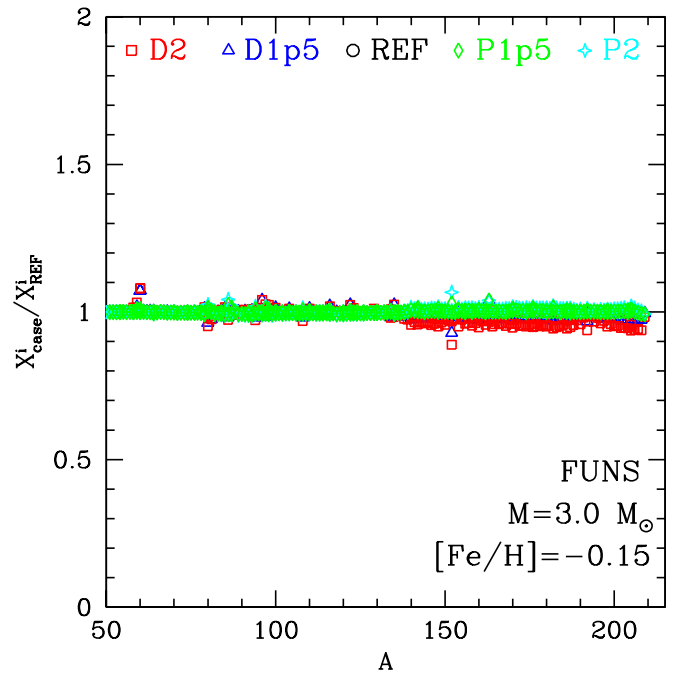


Figure 6. Same as Figure 5, but for the isotopic composition.

physical evolution of the model must be coupled to a full nuclear network, including all chemical species up to lead (see also Cristallo et al. 2016). This derives from the fact that, before the splitting (and the full development of the TP), the  $^{13}\text{C}(\alpha,n)^{16}\text{O}$  reaction provides a substantial fraction of the local energy budget. This reaction, in fact, directly releases about 2.2 MeV. Furthermore, an additional energy contribution comes from the following neutron capture (5 MeV, on average). It is therefore obvious that any model aiming at following a PIE cannot overlook the proper calculation of the energetics provided by neutron captures. The number of available neutrons depends on two factors: the mixing efficiency and the burning efficiency. In this paper, we test the latter by modifying the rate of the  $^{13}\text{C}(\alpha,n)^{16}\text{O}$  reaction.

However, before discussing our results, some important remarks about mixing have to be highlighted. First, it has to be stressed that the simulation of a three-dimensional hydrodynamic event, such as a PIE, in a one-dimensional hydrostatic code intrinsically implies the adoption of approximations. A key quantity in stellar evolution is the Damköhler number  $Da = \tau_{\text{mix}}/\tau_{\text{burn}}$  between the characteristic timescales of convective mixing ( $\tau_{\text{mix}}$ ) and nuclear burning ( $\tau_{\text{burn}}$ ). In the large majority of steady burning phases of a stellar evolution,  $Da \ll 1$  inside convective zones. During a PIE, instead,  $Da \rightarrow 1$ ; i.e., nuclear burning occurs “on the fly” (at least for hydrogen). As a first consequence, the model timestep ( $\Delta t$ ) needs to be reduced to follow the in-flight burning. In our models, we limit the timestep to 50% of the mixing turnover timescale of the convective shell ( $\tau_{\text{mix}}$ ), in order to avoid the unrealistic full homogenization of that region. All isotopes are mixed within the convective region, apart from protons, which are mixed down to the mass coordinate where  $\tau_{\text{burn}} = 1/3 \cdot \Delta t$  (see Cristallo et al. 2009b for details). At deeper coordinates,  $Da \gg 1$ ; i.e., the proton reduction (via nuclear burning) is much more rapid than the supply (via convective mixing). As a consequence, below this point, it is unlikely for protons to survive. Other approaches, however, may be implemented, possibly leading to

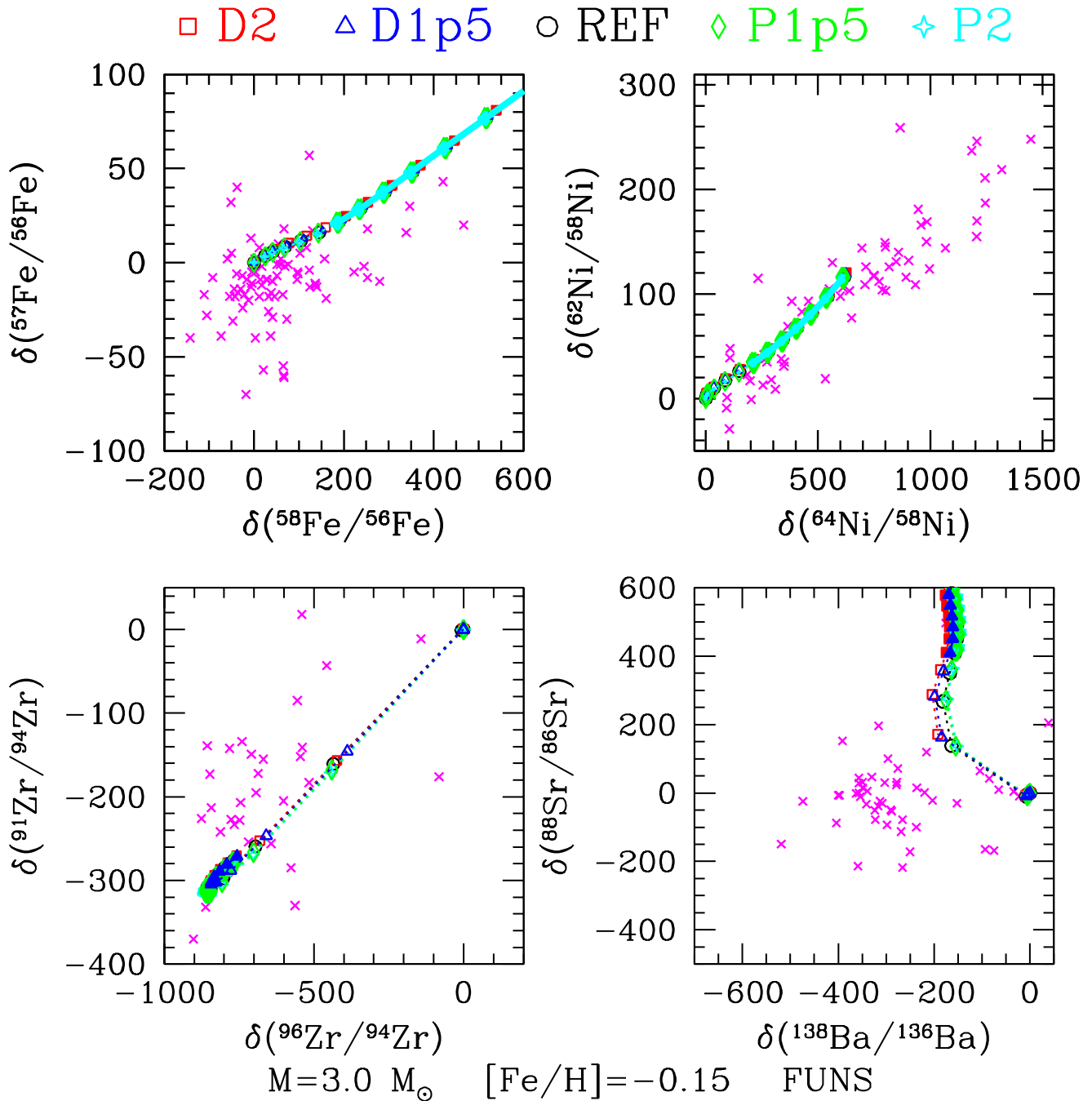


Figure 7. Same as Figure 4, but for a star with initial mass  $M = 3 M_{\odot}$ .

different results. For instance, Campbell & Lattanzio (2008) followed a diffusive approach in their calculation of PIEs. Diffusion being a very efficient mixing mechanism, the adoption of a diffusion equation in their code leads to an early splitting of the convective region. This has strong consequences for the following  $s$ -process nucleosynthesis (strongly hampering it).

Second, we stress that in our code, the rate of mixing is calculated basing on the mixing-length theory (MLT). This is a very crude approximation, since the MLT is a local theory and cannot capture the three-dimensional hydrodynamic nature of a PIE. In particular, the inhomogeneities in the flow and their effect on the three-dimensional distribution of burning cannot be taken into account. Moreover, the MLT cannot treat

macroscopic motions, such as the Global Non-spherical Oscillations (GOSH) for H-ingestion flashes described by Herwig et al. (2014). Due to the huge computer time requested, those simulations can be used to constrain one-dimensional hydrostatic calculations, but they cannot substitute them yet. Then, we reckon that explorations such as the one presented here still herald precious hints on the physics of PIEs, and, thus, we proceed in describing our result.

In Figure 9, we report the heavy-element surface distributions of a  $1.3 M_{\odot}$  model with  $[\text{Fe}/\text{H}] = -2.85$ . A dichotomy clearly emerges. The three cases with a high  $^{13}\text{C}(\alpha, n)^{16}\text{O}$  rate (P2, P1p5, and REF) show similar distributions, even if they have important exceptions (see, e.g., lead and bismuth). On the

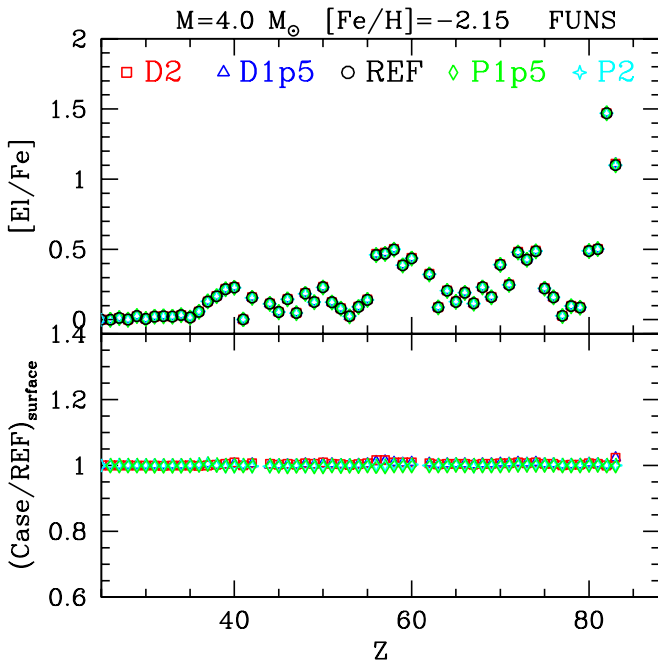


**Figure 8.** Same as Figure 2, but for a star with initial mass  $M = 4 M_{\odot}$  and  $[\text{Fe}/\text{H}] = -2.15$ .

contrary, other cases (D1p5 and D2) display a completely different behavior, with a definitely lower production of heavy elements (more than a factor of 50). Thus, it looks like the variation of the  $^{13}\text{C}(\alpha, n)^{16}\text{O}$  rate induces a sort of threshold effect in the  $s$ -process nucleosynthesis of this model. This is well understood in the framework of the PIE mechanism. Once the shell has split, the nucleosynthesis of the two shells follows separate evolutions. The lower one consumes its  $^{13}\text{C}$  reservoir, for a while in a convective environment and later on, when convection has switched off, in a radiative way. The upper shell instead continuously ingests protons, producing a large amount of  $^{13}\text{C}$ , as well as  $^{14}\text{N}$  (which acts as a poison). As a consequence, the production of heavy elements in the upper shell almost freezes after the splitting. As soon as the H-burning switches off, the convective envelope penetrates inward up to the splitting coordinate, carrying to the surface the material processed in the upper shell. On the contrary, the  $s$ -process-rich material of the lower shell is diluted in the following TP, and it is mixed to the surface at the epoch of the following TDU episode. Later, the model follows a standard AGB evolution. The two cases with a reduced  $^{13}\text{C}(\alpha, n)^{16}\text{O}$  rate ingest protons as well, but the splitting occurs before enough  $^{13}\text{C}$  has been mixed to the bottom of the convective shell (and, thus, an efficient  $s$ -process nucleosynthesis has developed). In Figure 10, we report the maximum neutron densities attained at the base of the convective shell for the different adopted rates as a function of the time since the beginning of the PIE. It is evident that the D1p5 and D2 cases attain lower neutron densities ( $\sim 10^{13} \text{ cm}^{-3}$  compared to  $\sim 10^{15} \text{ cm}^{-3}$ ) and, consequently, the following  $s$ -process enhancement is lower. The corresponding  $s$ -process indexes  $[\text{hs}/\text{ls}]^{19}$  and  $[\text{Pb}/\text{hs}]$  are reported in Table 2 (see discussion in Section 5).

<sup>19</sup>  $[\text{hs}/\text{ls}] = [\text{hs}/\text{Fe}] - [\text{ls}/\text{Fe}]$ , where  $[\text{ls}/\text{Fe}] = ([\text{Sr}/\text{Fe}] + [\text{Y}/\text{Fe}] + [\text{Zr}/\text{Fe}])/3$  and  $[\text{hs}/\text{Fe}] = ([\text{Ba}/\text{Fe}] + [\text{La}/\text{Fe}] + [\text{Nd}/\text{Fe}] + [\text{Sm}/\text{Fe}])/4$ .

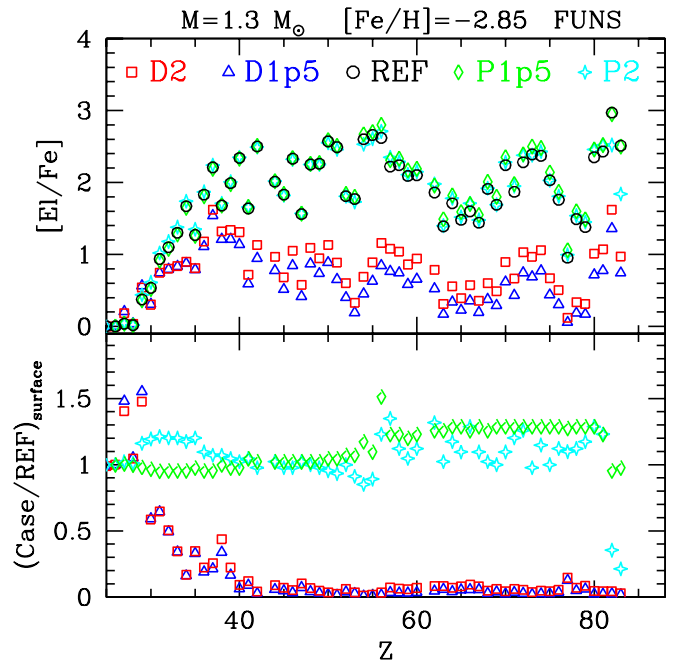


**Figure 9.** Same as Figure 2, but for a star with initial mass  $M = 1.3 M_{\odot}$  and  $[\text{Fe}/\text{H}] = -2.85$ .

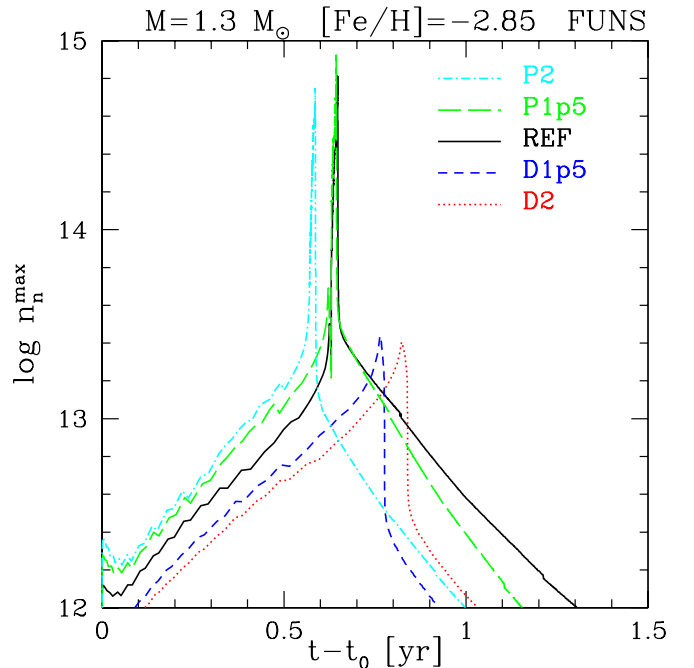


**Figure 10.** Neutron densities attained during the PIE of a star with  $M = 1.3 M_{\odot}$  and  $[\text{Fe}/\text{H}] = -2.85$  as a function of different rates for the  $^{13}\text{C}(\alpha, n)^{16}\text{O}$  reaction.

### 3.2. NEWTON Models

The NEWTON code calculates  $s$ -process nucleosynthesis for low-mass AGB stars considering the contributions of both the  $^{13}\text{C}(\alpha, n)^{16}\text{O}$  neutron source and the  $^{22}\text{Ne}(\alpha, n)^{25}\text{Mg}$  one. It uses a network with 404 nuclei (from hydrogen to bismuth). As already highlighted in the Introduction, the formation of the  $^{13}\text{C}$  pocket is assumed to be induced by the stellar dynamo. By using the approach proposed by Nucci & Busso (2014), the proton penetration into the He-rich layers results in the

**Table 2**  
*s*-process Indexes of the  $1.3 M_{\odot}$  Model with  $[\text{Fe}/\text{H}] = -2.85$  for Different Values of the  $^{13}\text{C}(\alpha, n)^{16}\text{O}$  Reaction Rate

Case	[hs/l <sub>s</sub> ]	[Pb/hs]
D2	-0.33	0.63
D1p5	-0.49	0.66
REF	0.13	0.84
P1p5	0.23	0.63
P2	0.21	0.29

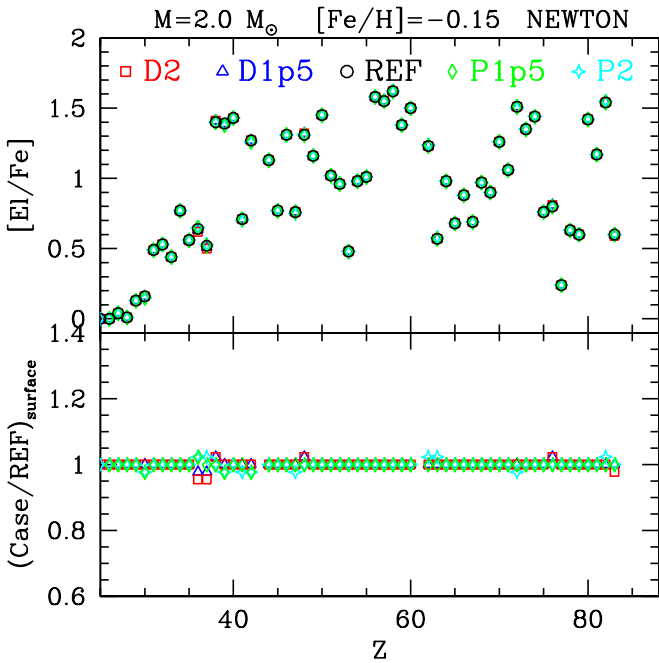


**Figure 11.** Same as Figure 2, but for a star with initial mass  $M = 2 M_{\odot}$  and  $[\text{Fe}/\text{H}] = -0.15$ .

advection to the envelope of the magnetized material from the inner radiative layers: as a consequence, the  $^{13}\text{C}$  reservoir formed is large (up to  $5 \times 10^{-3} M_{\odot}$ ) with an almost flat profile. Such a profile is quite different from the exponentially decreasing trend assumed in several other models (see, e.g., the EVEP mixing), while the  $^{14}\text{N}$  abundance is high in just a very thin layer adjacent to the envelope. Trippella et al. (2016) first showed that the neutron source  $^{13}\text{C}$  formed by MHD processes can account for the abundances of the main *s*-component nuclei in solar proportions, as well as the abundance distribution of post-AGB objects. In the same way, Palmerini et al. (2018) demonstrated that the magnetic mixing model, applied to a set of low-mass AGB stars (with masses from  $1.5$  to  $3 M_{\odot}$  and metallicities from  $1/3$  to  $1 Z_{\odot}$ ), provides a satisfactory explanation for the *s*-element isotopic mix measured in pre-solar SiC grains.

As in previous sections, we discuss here the effect induced on NEWTON nucleosynthesis predictions by a change of the  $^{13}\text{C}(\alpha, n)^{16}\text{O}$  reaction rate on a model of  $2.0 M_{\odot}$  and  $[\text{Fe}/\text{H}] = -0.15$ .<sup>20</sup> The reaction rates adopted for the  $^{13}\text{C}(\alpha, n)^{16}\text{O}$  reaction (Heil et al. 2008 divided and multiplied for factors

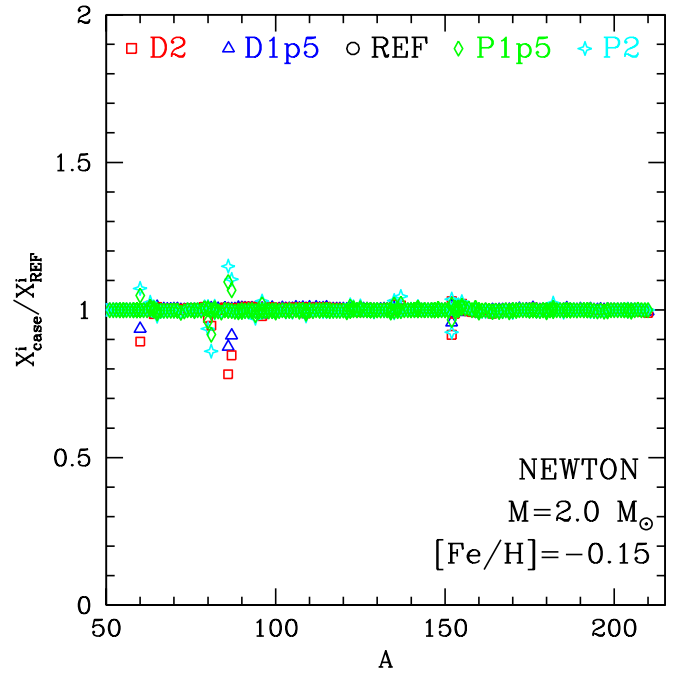


**Figure 12.** Same as Figure 11, but for the isotopic composition.

of 1.5 and 2) and the notation are the same as in the previous sections, as are as the SiC grain data used for comparison.

In Figures 11 and 12, the heavy-element surface composition and corresponding isotopic distribution of the  $2.0 M_{\odot}$  AGB star considered are reported for the five different choices of the  $^{13}\text{C}(\alpha, n)^{16}\text{O}$  reaction rate. Both the surface elemental composition and the isotopic one reveal no sensitivity to the  $^{13}\text{C} + \alpha$  cross section adopted in the calculations except for a few nuclei, namely  $^{60}\text{Fe}$ ,  $^{81}\text{Kr}$ ,  $^{86}\text{Kr}$ ,  $^{87}\text{Rb}$ , and  $^{96}\text{Zr}$ , whose abundance variations in any case range between 5% and 20%. The lower sensitivity of NEWTON to the  $^{13}\text{C}(\alpha, n)^{16}\text{O}$  reaction rate with respect to FUNS models is due to the fact that the  $^{13}\text{C}$  in the pocket is entirely consumed during the interpulse period. Thus, none is left to be burned in the convective shell triggered by the following TP for any choice of reaction rate. This is ascribed to the different stellar structure adopted to compute the post-process calculation with respect to the FUNS models described in the previous section. NEWTON models, in fact, use physical inputs computed with the FRANEC code (Straniero et al. 2003), in which the exponentially decaying profile of convective velocities was not implemented. Therefore, the core mass  $M_{\text{H}}$  at the first TP followed by TDU is larger for any computed model. For instance, in the  $2.0 M_{\odot}$  studied here,  $M_{\text{H}} \sim 0.61$ , to be compared with the typical values characterizing FUNS models ( $M_{\text{H}} \sim 0.56$ ; see previous section). In Figure 13, we repeat the comparison between isotopic ratios found in pre-solar SiC grains and the theoretical predictions of the NEWTON code for the *s*-process nucleosynthesis of the  $2.0 M_{\odot}$  AGB model. No remarkable changes are yielded by the  $^{13}\text{C}(\alpha, n)^{16}\text{O}$  reaction rate adopted in the calculation. However, we highlight the different trends of the curves in this figure and the ones of Figures 4 and 7, which do not depend on the nuclear physics input but on the physical mechanism responsible for the  $^{13}\text{C}$  pocket formation.

<sup>20</sup> Note that the effects of a variation of the  $^{13}\text{C}(\alpha, n)^{16}\text{O}$  reaction in the  $1.5$  and  $3.0 M_{\odot}$  models have already been presented by Trippella & La Cognata (2017).

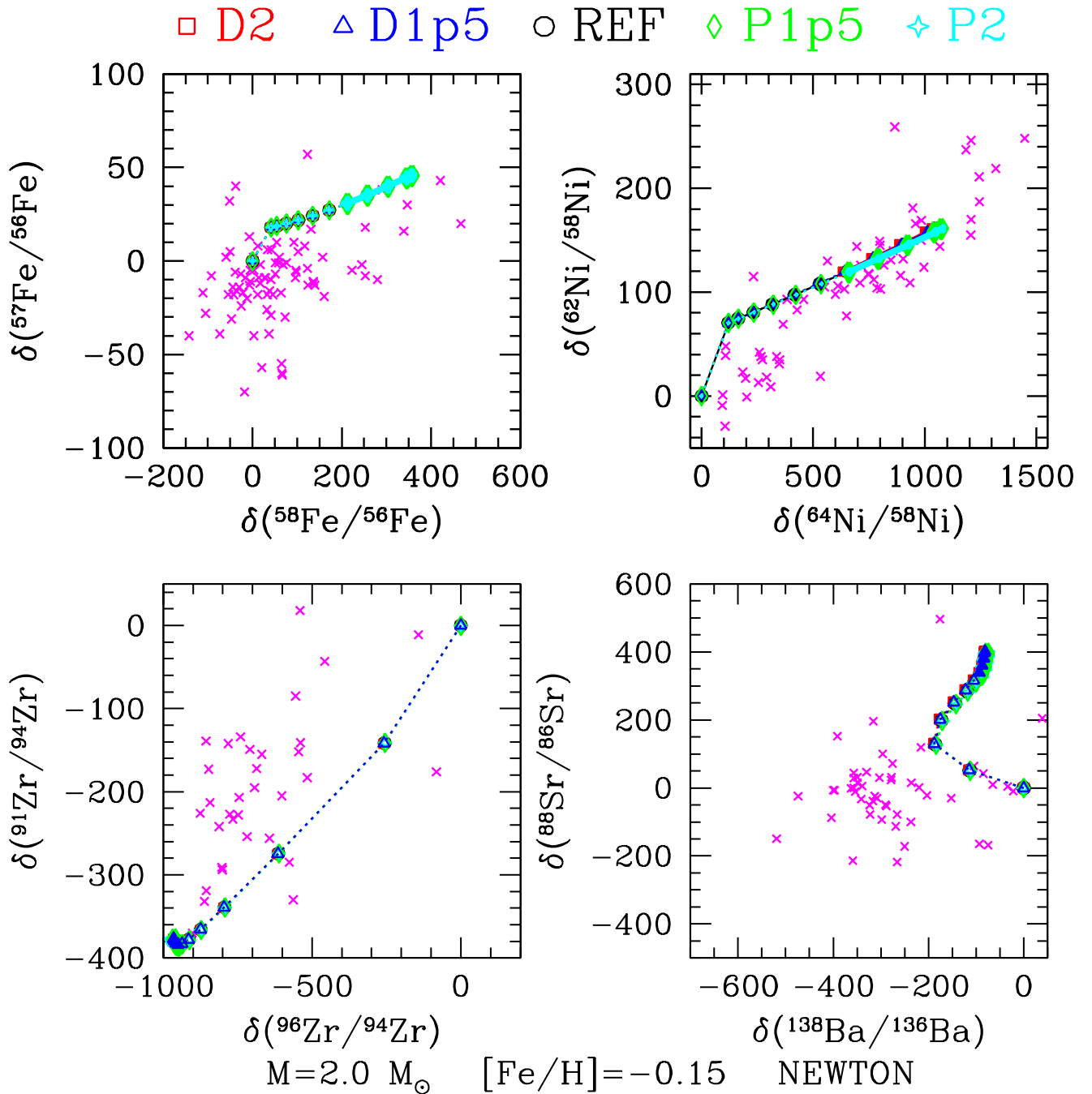


Figure 13. Same as Figure 11, but for the isotopic composition.

#### 4. Future Perspectives

The theoretical results presented in the previous section, as well as the discussion of the experimental status of the  $^{13}\text{C}(\alpha, n)^{16}\text{O}$  reaction reported in Section 2, clearly call for further direct measurements of its  $S$ -factor within the Gamow window corresponding to a radiative  $^{13}\text{C}$  burning. Owing to the vanishingly small cross section, it is then very likely that only underground measurements can help to sort out the discrepancies affecting direct data on the  $^{13}\text{C}(\alpha, n)^{16}\text{O}$  reaction, provided that the neutron detection efficiency of the setup is accurately known. The application of underground facilities to its investigation is detailed in Section 4.1.

Alternative approaches would also help to clarify the contradictory results brought by direct and indirect methods. In particular, the use of the detailed balance theorem (Section 4.2) might be of great help as an independent indirect technique, since the  $^{13}\text{C}(\alpha, n)^{16}\text{O}$  cross section could be obtained with no need of neutron detectors, reducing possible sources of systematic errors linked to the detection of neutrons.

##### 4.1. The LUNA Experiment

In order to tackle the very challenging direct measurement of the low-energy cross section, the signal-to-background ratio needs to be as high as possible. The main limitation of the

previous experiments that went the lowest in energy (Drotleff et al. 1993; Heil et al. 2008) was the natural background radiation, which at low enough energies (and with that, cross sections) becomes too dominant to allow further continuation toward the Gamow peak for radiative  $^{13}\text{C}$  burning.

Since the detection efficiency of the setups and the beam currents impinging the targets were already rather high, only small signal rate gains of maybe up to an order of magnitude can be achieved by improving these aspects of the measurement. Further improvement on the state of the art of direct measurements seems to be only possible through a drastic suppression of the environmental backgrounds.

In deep underground laboratories like the Gran Sasso National Laboratories (LNGS), both the cosmic-ray-induced  $\gamma$ -ray and neutron backgrounds are drastically reduced with respect to the surface:  $\gamma$ -rays by about six and (thermal) neutrons by up to three orders of magnitude (Best et al. 2016a, 2016b). The Laboratory for Underground Nuclear Astrophysics (LUNA) at the LNGS has for over 25 yr exploited the low-background conditions underground to measure astrophysical relevant nuclear reaction cross sections close to or directly inside the relevant stellar burning energies (see Best et al. 2016b and references therein). The LUNA 400 accelerator (Formicola et al. 2003) can provide 50–400 keV proton and  $\alpha$ -beams with currents up to around 400  $\mu\text{A}$ , covering the energy range of interest for this reaction. To successfully measure the very low cross sections in the astrophysical energy range, LUNA will use a high-efficiency detector made of  $^3\text{He}$  counters embedded in a moderating polyethylene matrix (a proven design used in many experiments in the past; see, e.g., Falahat et al. 2013 and references therein). At the low expected count rates (a few neutrons per day at the lowest energies), the internal  $\alpha$ -activity of the counters themselves becomes a relevant background (Hashemi-Nezhad & Peak 1998). It will be suppressed using pulse-shape discrimination methods (Langford et al. 2013), further improving the signal-to-background ratio.

The measurement of  $^{13}\text{C}(\alpha, n)^{16}\text{O}$  is also on the list of reactions to be measured with a second high-energy accelerator to be installed at LNGS, LUNA MV. The energy range covered by this new device is from 200 kV to 3.5 MV, providing an overlap region with the LUNA 400 keV (the accelerator currently used). The LUNA MV will connect the low-energy data to the higher-energy region, allowing an additional cross-check of the systematic uncertainties. The extended data set will also provide very valuable information for a global analysis using, for example, an R Matrix approach.

In summary, the LUNA experiment aims at a direct measurement of the cross section of the  $^{13}\text{C}(\alpha, n)^{16}\text{O}$  reaction at the Gamow energy for radiative  $^{13}\text{C}$  burning. Based on preliminary studies of the intrinsic activity of the detector and laboratory background, it appears realistic to map out the reaction down to  $\approx 250$  keV in the center-of-mass system. The lowest-energy data points will—after a few weeks of data taking—reach precisions high enough to much better constrain the cross section in the Gamow energy window than it currently is. The reduction of the uncertainty of the reaction rate will help—in combination with other direct data, from the LUNA MV and other sources, and indirect data—to resolve the open astrophysical questions outlined in the Introduction of this paper.

#### 4.2. The $n_{\text{TOF}}$ Experiment

As already discussed above, when the direct approach to the study of  $(\alpha, n)$  reactions is particularly difficult, indirect or inverse reactions are considered as a valid method for constraining the reaction cross sections of astrophysical interest. For instance, at the  $n_{\text{TOF}}$  facility at CERN (Guerrero et al. 2013), an important contribution to the study of the  $^{22}\text{Ne}(\alpha, n)^{25}\text{Mg}$  neutron source was recently provided on the basis of neutron spectroscopy of  $^{26}\text{Mg}$  states (Massimi et al. 2017).

The challenging  $^{13}\text{C}(\alpha, n)^{16}\text{O}$  measurement can benefit from experimental information from the time-reversed reaction  $^{16}\text{O}(n, \alpha)^{13}\text{C}$ . In particular, by using the detailed balance (i.e., time-reversal invariance theorem), the reaction cross section of  $^{13}\text{C}(\alpha, n)^{16}\text{O}$  is deduced from the measurement in the reverse direction. As shown in Figure 1, the nuclear reaction is a two-step process: first, an excited state of the  $^{17}\text{O}$  compound nucleus is populated, and, after, it decays into an exit channel. Since any excited state is characterized by its spin and parity, another interesting relation between direct and inverse reaction arises: the value of the channel spin of the entrance ( $^{16}\text{O}+n$ ) and the exit channel ( $^{13}\text{C}+\alpha$ ) is the same,  $\hbar/2$ , but the parity is opposite. As a consequence, if the formation of a resonant state is possible via  $s$ -wave neutrons ( $\ell = 0$ ), it cannot be formed via  $s$ -wave  $\alpha$ -particles, and it can occur most probably via  $p$ -wave. In summary, besides the Coulomb barrier, which strongly suppresses the cross section of the direct reaction at low energy and does not affect the inverse reaction, the orbital angular momentum can also play a role in the suppression or enhancement of the resonance cross section. The  $\alpha$ -unbound states of  $^{17}\text{O}$  can be studied by impinging a neutron beam on a  $^{16}\text{O}$  target. Because of the difference of about 2.22 MeV in the  $Q$ -value of the direct and inverse reaction, the threshold neutron energy of the  $^{16}\text{O}(n, \alpha)^{13}\text{C}$  reaction is about 2.35 MeV. This kind of measurement will be performed at the neutron time-of-flight ( $n_{\text{TOF}}$ ) facility of CERN. In particular, thanks to its excellent energy resolution and high neutron flux, the  $n_{\text{TOF}}$  facility offers the opportunity to perform such a measurement at a sufficiently large number of energies and to resolve fine structures in the cross section. The  $n_{\text{TOF}}$  EAR1 experimental area is placed at a distance of about 185 m from the spallation target, and it is best suited for high-precision measurements thanks to its excellent energy resolution ( $\Delta E/E = 5.3 \times 10^{-3}$  at  $E_n = 1$  MeV), which allows us to perform a precise resonance shape analysis.

The detection setup consists of a double Frisch grid ionization chamber with a common cathode. All the material in-beam has been kept to a minimum so as to reduce the effect due to the in-beam  $\gamma$ -ray burst generated by the spallation reactions. The gas mixture is composed of Kr(95%) +  $\text{CO}_2$ (5%), where the latter acts as the oxygen sample itself. The use of an ionization chamber with the gas acting also as a target allows one to detect  $\alpha$ -particles with energy as low as a few hundred keV, since the full particle energy is released inside the active volume of the detector. As a consequence, it may well be possible with this technique to observe and characterize the first few levels above the  $\alpha$ -threshold. For instance, the time-reversal measurement planned at the  $n_{\text{TOF}}$  facility may provide additional information on the  $5/2^+$  (at  $E_x = 7.164$  MeV, corresponding to  $E_n = 3.21$  MeV) and  $7/2^-$  (at  $E_x = 7.318$  MeV, corresponding to  $E_n = 3.44$  MeV) states, corresponding to  $\alpha$ -particle energies of 500 and 700 keV.

## 5. Discussion and Conclusions

The sensitivity study performed in this work heralds interesting results that further strengthen the need of more detailed nuclear data concerning the  $^{13}\text{C}(\alpha,n)^{16}\text{O}$  cross section. In order to evaluate the effect on  $s$ -process nucleosynthesis induced by the use of any of the  $^{13}\text{C}(\alpha,n)^{16}\text{O}$  rates currently available in the literature, our study focused on a theoretical range well beyond the most recent uncertainty estimates. First, we carefully scrutinized the pool of experimental data regarding the  $^{13}\text{C}(\alpha,n)^{16}\text{O}$  cross section to find the uncertainty affecting the corresponding reaction rate. Owing to the large scatter in direct measurements, discrepancies as large as a factor of 2 are apparent in the absolute value of the cross section and then in the calculated reaction rate (see Section 2), while an average error of 25% has been calculated by taking into account all available data sets (see Trippella & La Cognata 2017). Therefore, we varied by a factor of 1.5 and 2 (upward and downward) the rate proposed by Heil et al. (2008), assumed as a reference case, to include potential systematic errors. The most interesting results are as follows:

1. A variation of the  $^{13}\text{C}(\alpha,n)^{16}\text{O}$  rate does not appreciably affect  $s$ -process distributions for masses above  $3 M_{\odot}$  at any metallicity. The results obtained with the NETWON post-process code and the FUNS evolutionary code are consistent among them. Apart from a few isotopes, the differences derived from a variation of the  $^{13}\text{C}(\alpha,n)^{16}\text{O}$  reaction are always below 5%. This basically confirms the previous finding by Guo et al. (2012) and Trippella & La Cognata (2017).
2. The situation is completely different if the standard paradigm of the  $s$ -process (i.e., that all  $^{13}\text{C}$  within the pockets burns radiatively) is violated. This occurs in FUNS models of low mass ( $M < 3 M_{\odot}$ ) at solar-like metallicities (Cristallo et al. 2009a; see also Karakas et al. 2010). In such a case, a change of the  $^{13}\text{C}(\alpha,n)^{16}\text{O}$  reaction rate leads to nonnegligible variations in both the elemental and isotopic composition of the model. On average, the element surface distribution differs by about 10% with respect to the reference model, the heavier species showing the largest variations. A peak of 30% is obtained for rubidium: this is a consequence of the large overproduction (underproduction) of  $^{87}\text{Rb}$  for slower (faster) reaction rates. Such a trend is also found for other neutron-rich isotopes, such as  $^{60}\text{Fe}$  (a factor of 20). Unfortunately, the typical uncertainties affecting the spectra of  $s$ -process-rich stars are beyond the expected theoretical variations. Our analysis can safely discard extremely low values for the  $^{13}\text{C}(\alpha,n)^{16}\text{O}$  rate only. More precise constraints can be extracted from pre-solar SiC grain data. A change of the  $^{13}\text{C}(\alpha,n)^{16}\text{O}$  reaction rate within the explored range produces substantial differences in the isotopic surface ratios, in particular for the zirconium isotopes. However, the intrinsic spread characterizing SiC grains does not allow us to draw any firm conclusions. Larger  $^{13}\text{C}(\alpha,n)^{16}\text{O}$  rates also produce larger surface  $^{86}\text{Kr}/^{82}\text{Kr}$  isotopic ratios. Even if this result is going in the right direction, the extreme ratios ( $\sim 3$ ) found by Verchovsky et al. (2004) cannot be matched. Therefore, we confirm the results by Guo et al. (2012).
3. The by far more interesting result comes from low-mass, low-metallicity FUNS models ( $M = 1.3 M_{\odot}$  with  $[\text{Fe}/\text{H}] = -2.85$ ). In this case, during the first fully developed TP, some protons are engulfed in the underlying convective shell and burn on the fly (PIE). During this peculiar phase, characterized by an extraordinarily rich nucleosynthesis, the energy budget results from the balance between H-burning and He-burning. The latter receives an important energetic contribution from the  $^{13}\text{C}(\alpha,n)^{16}\text{O}$  reaction. Depending on the adopted rate, completely different results are attained. In particular, the surface abundances of the heavier elements may decrease by more than a factor of 50 when slow rates for the  $^{13}\text{C}(\alpha,n)^{16}\text{O}$  reaction are used. Our results are substantially different from those obtained by Guo et al. (2012). The reason lies in the different approaches to the modeling of proton ingestions. In Guo et al. (2012), a post-process technique has been applied to follow the ongoing  $s$ -process nucleosynthesis. In such a case, any energetic feedback from the  $^{13}\text{C}(\alpha,n)^{16}\text{O}$  reaction and, most important, from the following neutron capture is lost. It has been demonstrated in the past that the physical evolution of the model strongly depends on that. The difference in the results follows consequently. Unfortunately, also in this case, observations cannot help in constraining the  $^{13}\text{C}(\alpha,n)^{16}\text{O}$  rate. In fact, halo stars showing  $s$ -process-enhanced distributions owe their surface compositions to pollution events from an already extinct AGB. From the pollution episode up to now, other mixing processes may have modified the observed distribution (such as gravitational settling; see, e.g., Stancliffe et al. 2007). Thus, we cannot take advantage of absolute abundances to derive firm conclusions. In principle, this problem can be circumvented by looking at the relative enhancement of the three  $s$ -process peaks. Observations indicate that, on average,  $[\text{hs}/\text{ls}] > 0.3$  (see, e.g., Figure 5 in Cristallo et al. 2016). These values are consistent with the numbers obtained with the highest  $^{13}\text{C}(\alpha,n)^{16}\text{O}$  reaction rates (REF, P1p5, and P2; see Table 2). On the other hand, there are some isolated stars showing very low  $[\text{hs}/\text{ls}]$  values ( $\sim -0.5$ ), which would be consistent with low rates (cases D1p5 and D2; see Table 2). Thus, if we base our reasoning on a mere probabilistic criterion, we should exclude the lowest rates. However, it has to be taken into account that the calculation of a PIE in a one-dimensional hydrostatic code involves many approximations, which are hard to verify (see, e.g., Herwig et al. 2014). Moreover, the occurrence itself of this peculiar type of mixing in low-mass, low-metallicity stars is still a matter of debate, since it strongly depends on the initial composition (and, in particular, on the initial enrichment of  $\alpha$ -elements). In conclusion, regardless of the robustness of the obtained results, we cannot get any hints on the efficiency of the  $^{13}\text{C}(\alpha,n)^{16}\text{O}$  reaction in those stars.

Current observational and laboratory uncertainties cause our attempt to constrain the  $^{13}\text{C}(\alpha,n)^{16}\text{O}$  rate by means of stellar models to be almost fruitless. In the future, however, very high-resolution spectrographs mounted on next-generation telescopes (e.g., HIRES on the E-ELT telescope; Marconi et al. 2016), as well as advanced resonant ionization mass spectrometers (e.g., CHARISMA; Savina et al. 2003), will provide extremely precise data (reducing the related errors and disentangling an eventual contamination from solar system material, respectively). In the

meantime, any improvement in our knowledge of the  $^{13}\text{C}(\alpha,n)^{16}\text{O}$  rate will be useful. The ongoing experimental effort illustrated in this work is expected to produce in the next years a new set of direct and indirect data on the  $^{13}\text{C}(\alpha,n)^{16}\text{O}$  reaction. The determination of its reaction rate will benefit from the crucial information from the direct measurement and take advantage of the additional constraints from indirect measurements (e.g., the strong sensitivity of THM to the  $^{17}\text{O}$  level near the  $\alpha$ -threshold). In addition, the combination of the direct  $^{13}\text{C}(\alpha,n)^{16}\text{O}$  data from LUNA and the inverse  $^{16}\text{O}(n,\alpha)^{13}\text{C}$  data from n\_TOF can be used to reduce any possible source of systematic uncertainties. In summary, an accurate characterization of the resonant structures in the  $^{13}\text{C}(\alpha,n)^{16}\text{O}$  reaction cross section in the energy region of interest can be attained. It will eventually constraint the reaction rate to a conclusive level, well below the limits considered in the present study.

S.P. acknowledges the support of Fondazione Cassa di Risparmio di Perugia.

### ORCID iDs

S. Cristallo  <https://orcid.org/0000-0001-9683-9406>  
 M. La Cognata  <https://orcid.org/0000-0002-1819-4814>  
 C. Massimi  <https://orcid.org/0000-0003-2499-5586>  
 O. Trippella  <https://orcid.org/0000-0002-4757-0487>  
 L. Piersanti  <https://orcid.org/0000-0002-8758-244X>  
 D. Vescovi  <https://orcid.org/0000-0003-0309-4666>

### References

- Astropy Collaboration, Robitaille, T. P., Tollerud, E. J., et al. 2013, *A&A*, **558**, A33
- Avila, M. L., Rogachev, G. V., Koshchiy, E., et al. 2015, *PhRvC*, **91**, 048801
- Bair, J. K., & Haas, F. X. 1973, *PhRvC*, **7**, 1356
- Battino, U., Pignatari, M., Ritter, C., et al. 2016, *ApJ*, **827**, 30
- Best, A., Caciolli, A., Fülöp, Zs., et al. 2016b, *EPJA*, **52**, 72
- Best, A., Göerres, J., Junker, M., et al. 2016a, *NIMPA*, **812**, 1
- Bisterzo, S., Gallino, R., Käppeler, F., et al. 2015, *MNRAS*, **449**, 506
- Bracci, L., Fiorentini, G., Melezhik, V. S., Mezzorani, G., & Quarati, P. 1990, *NuPhA*, **513**, 316
- Busso, M., Gallino, R., & Wasserburg, G. J. 1999, *ARA&A*, **37**, 239
- Busso, M., Lambert, D. L., Beglio, L., et al. 1995, *ApJ*, **446**, 775
- Busso, M., Picchio, G., Gallino, R., & Chieffi, A. 1988, *ApJ*, **326**, 196
- Campbell, S. W., & Lattanzio, J. C. 2008, *A&A*, **490**, 769
- Caughlan, G. R., & Fowler, W. A. 1988, *ANDDT*, **40**, 283
- Chieffi, S., & Straniero, O. 1989, *ApJ*, **71**, 47
- Cristallo, S., Karinkuzhi, D., Goswami, A., Piersanti, L., & Gobrecht, D. 2016, *ApJ*, **833**, 181
- Cristallo, S., Piersanti, L., Straniero, O., et al. 2009b, *PASA*, **26**, 139
- Cristallo, S., Piersanti, L., Straniero, O., et al. 2011, *ApJS*, **197**, 2
- Cristallo, S., Straniero, O., Gallino, R., et al. 2009a, *ApJ*, **696**, 797
- Cristallo, S., Straniero, O., Piersanti, L., & Gobrecht, D. 2015, *ApJS*, **219**, 21
- Davids, C. 1968, *NuPhA*, **110**, 619
- Denissenkov, P. A., & Tout, C. A. 2003, *MNRAS*, **340**, 722
- Drotleff, H. W., Denker, A., Knee, H., et al. 1993, *ApJ*, **414**, 735
- ENDFS 2017, International Network of Nuclear Structure and Decay Data Evaluators (<http://www-nds.iaea.org/nsdd/>)
- Faestermann, T., Mohr, P., Hertenberger, R., & Wirth, H.-F. 2015, *PhRvC*, **92**, 052802
- Falahat, S., Best, A., Couder, M., et al. 2013, *NIMPA*, **700**, 53
- Formicola, A., Imbriani, G., Junker, M., et al. 2003, *NIMPA*, **507**, 609
- Freytag, B., Ludwig, H.-G., & Steffen, M. 1996, *A&A*, **313**, 497
- Gallino, R., Arlandini, C., Busso, M., et al. 1998, *ApJ*, **497**, 388
- Goriely, S., & Mowlavi, N. 2000, *A&A*, **362**, 599
- Guandalini, R., & Cristallo, S. 2013, *A&A*, **555**, 120
- Guerrero, C., Tsinganis, A., Berthoumieux, E., et al. 2013, *EPJA*, **49**, 27
- Guo, B., Li, Z. H., Lugaro, M., et al. 2012, *ApJ*, **756**, 193
- Harissopulos, S., Becker, H. W., Hammer, J. W., et al. 2005, *PhRvC*, **72**, 062801
- Hashemi-Nezhad, S. R., & Peak, L. S. 1998, *NIMPA*, **416**, 100
- Heil, M., Detwiler, R., Azuma, R. E., et al. 2008, *PhRvC*, **78**, 025803
- Herwig, F. 2000, *A&A*, **360**, 952
- Herwig, F., Bloeker, T., Schoenberner, D., & El Eid, M. 1997, *A&A*, **324**, L81
- Herwig, F., Pignatari, M., Woodward, P. R., et al. 2011, *ApJ*, **727**, 89
- Herwig, F., Woodward, P. R., Lin, P.-H., Knox, M., & Fryer, C. 2014, *ApJL*, **792**, 3
- Iben, I., Jr., & Renzini, A. 1983, *ApJL*, **263**, 23
- Johnson, E. D., Rogachev, G. V., Mukhamedzhanov, A. M., et al. 2006, *PhRvL*, **97**, 192701
- Karakas, A., Campbell, S. W., & Stancliffe, R. J. 2010, *ApJ*, **713**, 374
- Keeley, N., Kemper, K. W., & Khoa, D. T. 2003, *NuPhA*, **726**, 159
- Kellogg, S., Vogelaar, R., & Kavanagh, R. 1989, *BAPS*, **34**, 1192
- Kubono, S., Abe, K., Kato, S., et al. 2003, *PhRvL*, **90**, 062501
- La Cognata, M., Spitaleri, C., & Mukhamedzhanov, A. M. 2010, *ApJ*, **723**, 1512
- La Cognata, M., Spitaleri, C., Trippella, O., et al. 2012, *PhRvL*, **109**, 232701
- La Cognata, M., Spitaleri, C., Trippella, O., et al. 2013, *ApJ*, **777**, 143
- Langer, N., Heger, A., Wellstein, S., & Herwig, F. 1999, *A&A*, **346**, L37
- Langford, T. J., Bass, C. D., Beise, E. J., et al. 2013, *NIMPA*, **717**, 51
- Liu, N., Gallino, R., Bisterzo, S., et al. 2014b, *ApJ*, **788**, 163
- Liu, N., Savina, M. R., Davis, A. M., et al. 2014a, *ApJ*, **786**, 66
- Liu, N., Savina, M. R., Gallino, R., et al. 2015, *ApJ*, **803**, 12
- Lugaro, M., Davis, A. M., Gallino, R., et al. 2003, *ApJ*, **593**, 486
- Marconi, A., Di Marcantonio, P., D'Odorico, V., et al. 2016, *Proc. SPIE*, **9908**, 23
- Massimi, C., Altstadt, S., Andrzejewski, J., et al. 2017, *PhLB*, **768**, 1
- Mezhevych, S. Yu., Rudchik, A. T., Rudchik, A. A., et al. 2017, *PhRvC*, **95**, 034607
- Mostefaoui, S., Lugmair, G. W., Hoppe, P., et al. 2005, *ApJ*, **625**, 271
- Mukhamedzhanov, A. M., Shubhchintak, & Bertulani, C. A. 2017, *PhRvC*, **96**, 024623
- Nucci, M. C., & Busso, M. 2014, *ApJ*, **787**, 141
- Palmerini, S., Trippella, O., Busso, M., et al. 2018, *GeCoA*, **221**, 21
- Parker, E. N. 1960, *ApJ*, **132**, 821
- Pellegriti, M. G., Hammache, F., Roussel, P., et al. 2008, *PhRvC*, **77**, 042801
- Piersanti, L., Cristallo, S., Straniero, O., et al. 2013, *ApJ*, **774**, 98
- Raut, R., Tonchev, A. P., Rusev, G., et al. 2013, *PhRvL*, **111**, 112501
- Savina, M. R., Pellin, M. J., Tripa, C. E., et al. 2003, *GeCoA*, **67**, 3215
- Schuessler, M. 1977, *A&A*, **56**, 439
- Shingles, L. J., Karakas, A. I., Hirschi, R., et al. 2014, *ApJ*, **795**, 34
- Spruit, H. C. 1999, *A&A*, **349**, 189
- Stancliffe, R. J., Glebbeek, E., Izzard, R. G., & Pols, O. R. 2007, *A&A*, **464**, 57
- Straniero, O., Cristallo, S., & Piersanti, L. 2014, *ApJ*, **785**, 77
- Straniero, O., Domínguez, I., Cristallo, S., & Gallino, R. 2003, *PASA*, **20**, 389
- Straniero, O., Gallino, R., Busso, M., et al. 1995, *ApJL*, **440**, 85
- Straniero, O., Gallino, R., & Cristallo, S. 2006, *NuPhA*, **777**, 311
- Tang, H., & Dauphas, N. 2012, *E&PSL*, **359**, 248
- Tilley, D. R., Weller, H. R., & Cheves, C. M. 1993, *NuPhA*, **564**, 1
- Trappitsch, R., Stephan, T., Savina, M. R., et al. 2018, *GeCoA*, **221**, 87
- Tribble, R. E., Bertulani, C. A., La Cognata, M., Mukhamedzhanov, A. M., & Spitaleri, C. 2014, *RPPH*, **77**, 106901
- Trippella, O., Busso, M., Palmerini, S., Maiorca, E., & Nucci, M. C. 2016, *ApJ*, **818**, 125
- Trippella, O., & La Cognata, M. 2017, *ApJ*, **837**, 41
- Verchovsky, A. B., Wright, I. P., & Pillinger, C. T. 2004, *ApJ*, **607**, 611
- Werner, K., & Herwig, F. 2007, *PASP*, **118**, 183